THE JOURNAL OF PHYSICAL CHEMISTRY C
A JOURNAL OF THE AMERICAN CHEMICAL SOCIETY

pubs.acs.org/JPCC

Article

First-Principles Modeling of Transport Mechanisms in Carbonate–Hydroxide Electrolytes

Published as part of The Journal of Physical Chemistry virtual special issue "Carol K. Hall Festschrift".

Anirban Mondal, Jeffrey M. Young, Gabor Kiss, and Athanassios Z. Panagiotopoulos*

Cite This: *J. Phys. Chem. C* 2021, 125, 4412–4422

Read Online

ACCESS | Metrics & More | Article Recommendations | Supporting Information

ABSTRACT: We performed *ab initio* molecular dynamics simulations of a molten $[Li_{0.6}K_{0.4}]_3CO_3OH$ electrolyte containing dissolved CO_2 and confirmed the presence of pyrocarbonate, bicarbonate, and water along with the constituent ions and molecular CO_2. Our calculations indicate kinetics-driven formation of pyrocarbonate whereas bicarbonate and water are thermodynamically favored. Our results also demonstrate the presence of water at higher concentrations (double or more) than that of CO_2, which reinforces the conclusions in our earlier work [*AIChE J.* **2020**, e16988] based on chemical reaction equilibrium simulations. Structural analysis indicates a larger distortion in water geometry, due to its higher polarizability compared to the nonpolar CO_2, explaining the higher reactivity and smaller average lifetime of H_2O in the melt. The computed lifetime distributions of the reaction products reveal that the bicarbonate ion lives the shortest among all the species present in the system. It initiates a sequence of successive proton exchange events; such sequences of exchanges along a hydrogen-bonded network gives the Grotthuss mechanism for proton transport in liquid water. The estimated proton diffusion, based on a random walk model, is about 30 times faster than the hydroxide diffusion obtained from classical molecular dynamics simulations. We believe that the presence of proton transfer events in the system has a large impact on the overall ion dynamics and electrical conductivity of the medium.

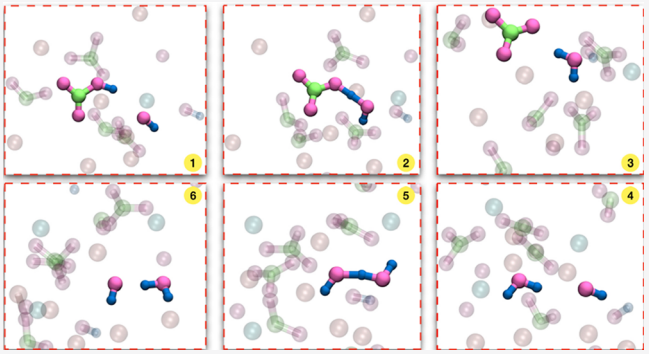

INTRODUCTION

Molten carbonates and their eutectic mixtures are promising materials for high-temperature thermal energy storage, for heat transfer applications, and as conducting electrolytes in molten carbonate fuel cells (MCFCs).[1] Of late, MCFCs have received increased attention in connection to distributed power generation and capturing CO_2 from flue gases. In MCFCs, a CO_2-containing gas is fed to the cathode, where CO_2 reacts with O_2 to yield carbonate (CO_3^{2-}) ions (eq 1). These ions are then transferred through the electrolyte to the anode, where they oxidize H_2 (eq 2) to produce electricity with high efficiency. When applied in carbon capture, the value of the electricity produced reduces the cost of carbon capture, making MCFCs one of the most promising technologies for the generation of clean energy from fossil fuels.[2,3]

$$\text{cathode:}\quad CO_2 + \frac{1}{2}O_2 + 2e^- \rightarrow CO_3^{2-} \tag{1}$$

$$\text{anode:}\quad H_2 + CO_3^{2-} \rightarrow H_2O + CO_2 + 2e^- \tag{2}$$

The electrolyte plays important roles in MCFCs. It acts as the solvent for all electrochemical half-reactions stabilizing the intermediates and transition states involved in the electrochemical process. MCFC electrolytes contain mixtures of Li/K or Li/Na carbonates near their eutectic compositions. In a working MCFC, the molten electrolyte is in contact with the cathode feed gas comprising CO_2, H_2O, and O_2. Consequently, the high-temperature ionic melt contains additional species in the electrolyte besides the dominant carbonate ions[4,5] due to chemical reactions between carbonate and dissolved species. One component that may be present in significant concentrations is hydroxide ions.[6−9] Hydroxide can affect the carbon capture efficiency of fuel cells as well as cause electrolyte loss.[10,11] Our recent computational study of chemical reaction equilibria[9] based on classical force fields revealed that substantial fractions of hydroxide ions can be present in alkali carbonate eutectic mixtures, provided that the partial pressure ratio of CO_2/H_2O over the molten salt is low,

Received: December 4, 2020
Revised: January 27, 2021
Published: February 19, 2021

https://dx.doi.org/10.1021/acs.jpcc.0c10879
J. Phys. Chem. C 2021, 125, 4412–4422

meaning that more water is present than CO_2, which is the case in carbon capture applications. These findings are consistent with recent experiments by Rosen et al.[8] that suggest a net consumption of water at the cathode, caused by water reacting with oxygen to produce hydroxide ions (eq 3) when operating at low CO_2 gas-phase concentration and high current density. Those hydroxide ions are then reduced at the anode (eq 4), creating an ion transport path parallel to the carbonate path in the MCFC. While this reaction sequence also transports oxygen and electrons from the cathode to the anode, it results in a net transport of H_2O rather than CO_2, resulting in a lower carbon capture efficiency at a given fuel utilization.

$$\frac{1}{2}O_2 + H_2O + 2e^- \rightarrow 2OH^- \quad (3)$$

$$2OH^- + H_2 \rightarrow 2H_2O + 2e^- \quad (4)$$

Besides the hydroxide, several activated oxygen species, including oxide, superoxide, and peroxide, are believed to be present in the electrolyte, and their formation is largely governed by the gas phase concentrations of CO_2, O_2, and water.[4,5,12,13] Recently, Corradini et al. reported the behavior of CO_2 in molten $CaCO_3$ by using *ab initio* molecular dynamics (AIMD) simulations.[14] They found a spontaneous reaction between CO_2 and a carbonate anion, yielding the pyrocarbonate ($C_2O_5^{2-}$) anion. In addition, the transport of CO_2 in molten $CaCO_3$ was shown to occur via a Grotthuss-like mechanism and was 3 times faster than the molecular diffusion. Because the MCFC electrolytes also contain significant fractions of hydroxide ions when in contact with wet cathode gas, the CO_2 present in the system may form bicarbonate (HCO_3^-) and other related species. As some or several of these entities could be key intermediates in the MCFC oxygen activation mechanism, it is worth exploring the different chemical routes for the formation of such species and estimating their relative proportions and stability in the molten electrolyte medium. Although our conclusions for chemical reaction equilibria in MCFCs based on classical molecular dynamics (MD) simulations have qualitatively rationalized the inconsistency between the charge and carbonate transfer balances in MCFCs,[8] those calculations did not take into consideration the potential reactive stabilization of CO_2 and H_2O with the anions. Despite their low concentrations in the electrolyte, these gases can form additional species upon reaction with carbonate and hydroxide ions. Moreover, the presence of HCO_3^- may have an additional role to play in the overall charge transport mechanism with the possibility of initiating a proton transfer channel as has been already suggested in several carbonate composite electrolytes used in the solid-oxide fuel cells.[15−17] Investigation of chemical reactions at the microscopic level requires an explicit description of the electronic degrees of freedom. To the best of our knowledge, there have been no prior publications of AIMD simulations in molten alkali-metal carbonate−hydroxide melts. The investigation of reactions and transport mechanisms in such melts forms the main objective of the current work.

In this study, we focus on the fate of CO_2 in a molten $[Li_{0.6}K_{0.4}]_3CO_3OH$ electrolyte to characterize the formation/dissociation of different chemical species derived from it and subsequently their role in altering the overall charge transport mechanism. This work is divided into four parts. Following the present introduction, we next describe the details of our AIMD simulations. We subsequently discuss our findings and their implications for transport in MCFCs. The final section of the paper presents our conclusions.

SIMULATION DETAILS

To investigate the chemical routes for the formation/dissociation of different chemical species and their role in the transport mechanism, we studied a system originally composed of 120 Li^+, 80 K^+, 80 CO_3^{2-}, 40 OH^- ions, and 10 CO_2 molecules. If the system is at equilibrium, the dissolved CO_2 concentration used here would correspond to unrealistically high gas phase partial pressure, as found in our earlier work based on chemical reaction equilibrium simulations.[9] The reason for imposing such a high initial CO_2 concentration was to improve the statistical accuracy of different quantities measured in this work, as these depend on the reaction of CO_2 with other molecules in the system. The temperature was set to 923.15 K, the experimentally measured melting point of the eutectic mixture, $[Li_{0.6}K_{0.4}]_3CO_3OH$.[18] To obtain a pre-equilibrated configuration at 923.15 K, we first performed classical MD simulations in the *NPT* ensemble at $P = 1$ bar using the GROMACS simulation program.[19,20] Details of the force field parameters and protocols are described elsewhere.[9,21,22]

The equilibrated supercell from the classical MD trajectory was geometry optimized within the density functional theory (DFT) framework at the same level of theory as described below. The gradients on the wave functions and on the nuclear positions were optimized with convergence criteria of 10^{-6} and 10^{-3} au, respectively. The quenched geometry was then used to set up Born−Oppenheimer MD simulations with the electronic structure code CP2K[23] by using the Quickstep module.[24] The exchange-correlation interactions were taken into account by the PBE functional.[25] Dispersive interaction corrections were included by utilizing the empirical dispersion correction (D3) from Grimme,[26] with a cutoff of 40 Å. All valence electrons were treated with the double-ζ valence plus polarization (DZVP) basis sets with an energy cutoff of 400 Ry. The norm-conserving Goedecker−Teter−Hutter (GTH)[27,28] pseudopotentials were applied to consider the effect of nuclei and core electrons. Equations of motion were integrated with a time step of 0.5 fs. The system was equilibrated for 8 ps in the isothermal−isobaric (*NPT*) ensemble at 1 bar by using an isotropic unit cell according to the scheme of Martyna et al.,[29] with a time constant of 250 fs. Equilibration was followed by a production simulation in the canonical *NVT* ensemble for 65 ps. We set the temperature at 923.15 K, controlled by one chain of six Nosé−Hoover thermostats[30] with a time constant of 100 fs. Three-dimensional periodic boundary conditions were employed in all simulations. The trajectory at every time step was stored for postsimulation analysis.

RESULTS AND DISCUSSION

Intermolecular reactions between the different species were probed by analyzing the relevant site−site radial distribution functions (RDFs). The trajectory is divided into 5 ps blocks, and RDFs were evaluated in each block to examine the changes in the intermolecular distributions. To observe the presence of reactions, the molecular identity corresponding to the initial frame, $t = 0$, was used to evaluate these RDFs. For example, the

https://dx.doi.org/10.1021/acs.jpcc.0c10879
J. Phys. Chem. C 2021, 125, 4412−4422

carbon atom of a carbonate anion at $t = 0$ is treated as it corresponds to carbonate always.

Pyrocarbonate Formation and Dissociation. Figure 1a exhibits the RDFs between the oxygen atoms of the original carbonate anions and the carbon atom of CO_2. The interesting feature here is the peak at around 1.38 Å, which is closer to the 1.42 Å C−O bond distance observed in the optimized gas phase geometry of the pyrocarbonate anion than to the 1.28 Å C−O bond distance in the carbonate anion, as shown in Figure S1 of the Supporting Information. Hence, this feature suggests the spontaneous formation of a pyrocarbonate anion as a result of the following chemical reaction:

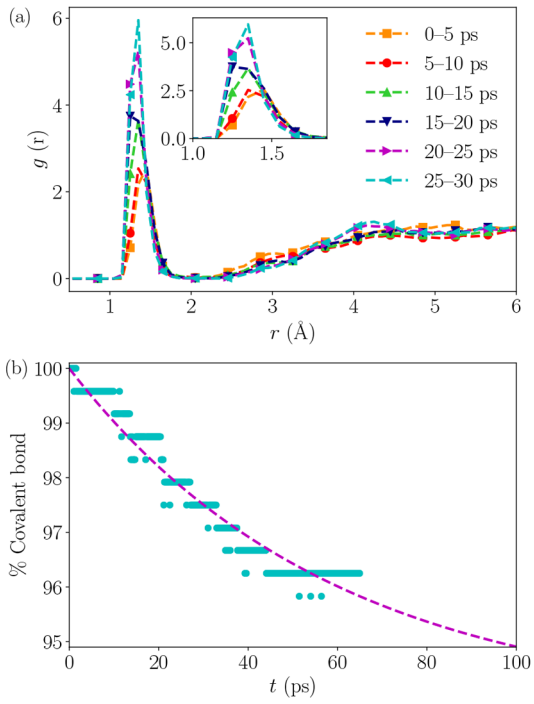

Figure 1. (a) Radial distribution functions between the carbon atom of CO_2 and oxygen atoms of CO_3^{2-}. (b) Percent covalent bond retained as a function of time: C−O bond in carbonate ions present at $t = 0$.

$$CO_2 + CO_3^{2-} \rightleftharpoons C_2O_5^{2-} \quad (5)$$

The initial absence of this peak (before 1 ps, see Figure S2) further substantiates the proposed reaction since this particular peak would not exist if there was no pyrocarbonate present in the medium. The peak height also shows a continuous growth as we progress in time, indicating an increase in the pyrocarbonate fraction over the simulation period.

To unravel the underlying mechanism of pyrocarbonate formation, we analyzed the AIMD trajectory. We observed the spontaneous formation and dissociation of pyrocarbonate ions from the reaction between CO_2 and CO_3^{2-}, as shown in Figure 2. The snapshots presented in Figure 2a−c show the approach of a CO_2 to a CO_3^{2-}, the pyrocarbonate that is formed, and its subsequent dissociation into a CO_3^{2-} and CO_2. We observed a near-instantaneous exchange between these species, with multiple instances of formation and dissociation of the pyrocarbonate ion. To further substantiate this observation, we computed the percent C−O covalent bond retained in original CO_3^{2-} ions as a function of time, which is shown in Figure 1b. This curve exhibits an exponential decay, implying that an oxygen atom originally in a CO_3^{2-} ion leaves its original carbon atom and becomes covalently bonded to a different carbon atom in the process of pyrocarbonate dissociation. Therefore, the identity of the C atoms belonging to a CO_2, CO_3^{2-}, or $C_2O_5^{2-}$ varies along the simulation trajectory. The same phenomenon was also reported by Corradini et al.[14] for CO_2 in molten calcium carbonate; however, the simulation temperature was much higher (1773 K) than in this study. Another key difference from that study is that in this work, since the molten electrolyte is composed of carbonate and hydroxide ions, CO_2 can also react with a OH^- ion. Therefore, unlike in molten $CaCO_3$, where CO_2 follows an oxo-Grotthuss transport via a pyrocarbonate anion, in molten alkali-metal carbonate−hydroxide electrolyte we expect multiple pathways of CO_2 transport. In the next section we investigate the interaction between CO_2 and hydroxide.

Bicarbonate Formation and Isomerization. RDFs between the oxygen center of hydroxide and the carbon atom of CO_2 are displayed in Figure 3a. Similar to Figure 1a, here again we observe the emergence of a peak at around 1.39 Å, similar to the 1.43 Å C−O bond length observed in the optimized gas phase geometry of bicarbonate (Figure S3). This indicates the spontaneous formation of the bicarbonate anion as a product of the following chemical reaction:

$$CO_2 + OH^- \rightleftharpoons HCO_3^- \quad (6)$$

More importantly, the peak corresponding to this newly formed covalent bond grows as a function of time and eventually exhibits a higher probability when compared to that of a similar peak (around 1.38 Å) in Figure 1a between CO_2

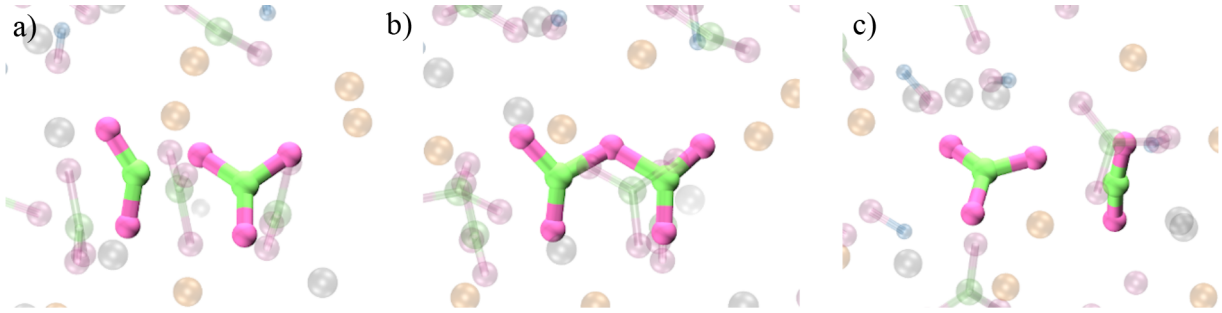

Figure 2. AIMD simulation snapshots representing one instance of the dynamic formation/dissociation of pyrocarbonate in the interaction between a carbonate ion and carbon dioxide: (a) CO_2 and CO_3^{2-} approach, (b) pyrocarbonate formed, and (c) pyrocarbonate dissociates into a CO_3^{2-} and a CO_2. Color scheme: C = lime; O = mauve. The rest of the atoms are shown as a transparent background for clarity.

https://dx.doi.org/10.1021/acs.jpcc.0c10879
J. Phys. Chem. C 2021, 125, 4412−4422

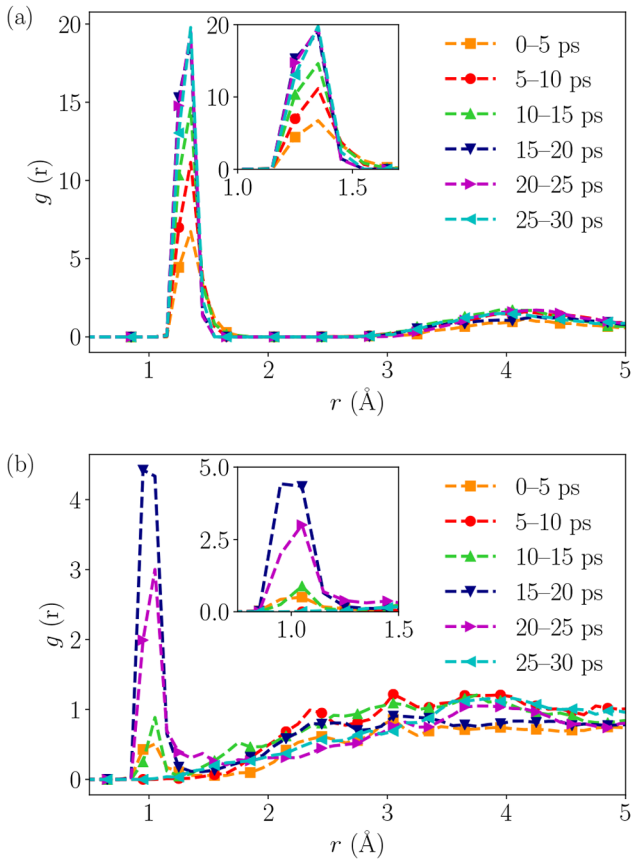

Figure 3. Radial distribution functions between (a) the carbon atom of CO_2 and the oxygen atom of OH^- and (b) the hydrogen atom of OH^- and the oxygen atoms of CO_2.

and CO_3^{2-} after the 5−10 ps time window. Therefore, we should expect a competition between carbonate and hydroxide ions reacting with CO_2, leading to the formation of pyrocarbonate and bicarbonate ions, respectively. Within 10 ps, it is evident that CO_2 preferentially forms bicarbonate over pyrocarbonate. This observation can be interpreted in terms of basicity order—CO_2, a Lewis acid, prefers stronger binding affinity with a stronger base, hydroxide, than the carbonate.[31]

We also examined the RDFs between the hydroxide hydrogen and the oxygens of CO_2, shown in Figure 3b. We note that the new peak emerging at 0.98 Å corresponds to intramolecular H transfer, a well-known phenomenon.[32,33] Analysis of the simulation trajectory reveals the spontaneous formation of a bicarbonate ion from the reaction between CO_2 and hydroxide (Figure 4). The snapshots displayed in Figure 4a−c show the approach of a CO_2 to a OH^-, the formed bicarbonate, and finally the exchange of the proton between two oxygen centers. The isomerization process as indicated by the RDFs in Figure 3b is thus manifested by these snapshots. It is not hard to speculate that the formed bicarbonate ion is highly polarizable in this medium and therefore may participate in subsequent reactions to follow.

Bicarbonate Dissociation and Water Formation. As discussed in the previous section, the bicarbonate ions follow a rapid dissociation reaction that involves a complete proton transfer from a HCO_3^- to a neighboring OH^- (Figure 5).

$$HCO_3^- + OH^- \rightleftharpoons CO_3^{2-} + H_2O \quad (7)$$

The reaction yields a carbonate and a molecular water as the product. The snapshots presented in Figure 5a−c depict the approach of a HCO_3^- to an OH^-, an adduct formed between bicarbonate and hydroxide, and the proton transfer from bicarbonate to hydroxide. Therefore, unlike the pyrocarbonate formation which contributed to CO_2 diffusion via an oxo-Grotthuss mechanism, bicarbonate formation does not lead to alternate pathways for CO_2 transport. Because the electrolyte medium is strongly basic in nature in the sense that it is composed of carbonate and hydroxide ions, the water molecules thus formed may not be stable for a long period of time and will undergo subsequent reactions. We probed the possibility of carbonate-induced polarization of bicarbonate (with proton transfer between bicarbonate and carbonate) by tracking the HCO_3^- throughout the trajectory. Interestingly, we observed adduct formation between a carbonate and a bicarbonate ion on more than one occasion. However, the proton never leaves the bicarbonate completely; instead, the proton is found to be shared between the two ions. It is worth mentioning here that the simulation time (70 ps) may not be long enough to attain an equilibrium, and thus complete transfer of a proton from a bicarbonate to another neighboring carbonate may still be feasible provided that we reach a longer time scales. This is outside the scope of this study.

Water-Mediated Proton Transfer. Figure 6a shows the RDFs between a hydrogen and oxygen of another hydroxide (intramolecular O−H bonds are neglected). As evident in the figure, for times up to 5 ps there is no sign of either the formation of a new covalent bond or dissociation of existing bonds (as confirmed from studying the intramolecular part in the RDF). Within the next 5 ps, a new peak begins to appear at around 0.98 Å and exhibits a continuous growth with time.

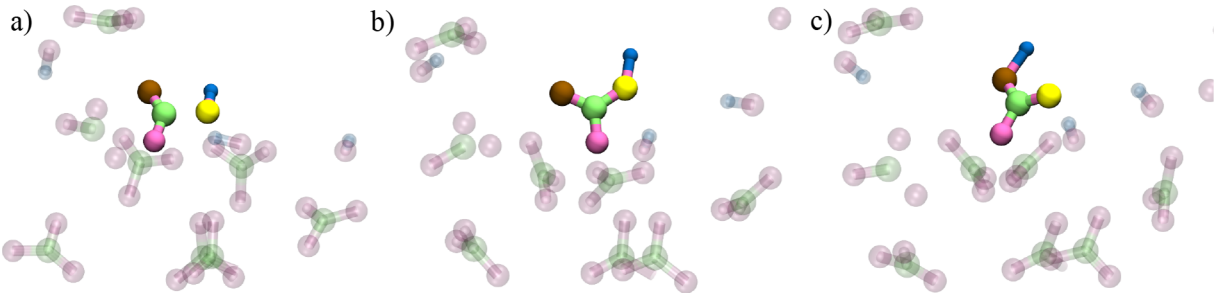

Figure 4. Snapshots representing one instance of the formation and isomerization of bicarbonate during AIMD simulation: (a) CO_2 and OH^- approach, (b) bicarbonate formed, and (c) proton exchange between adjacent oxygen atoms. Color scheme: C = lime; oxygen centers are shown in mauve, yellow, and ochre for better understanding; H = blue. The rest of the atoms are shown as a transparent background for clarity.

https://dx.doi.org/10.1021/acs.jpcc.0c10879
J. Phys. Chem. C 2021, 125, 4412−4422

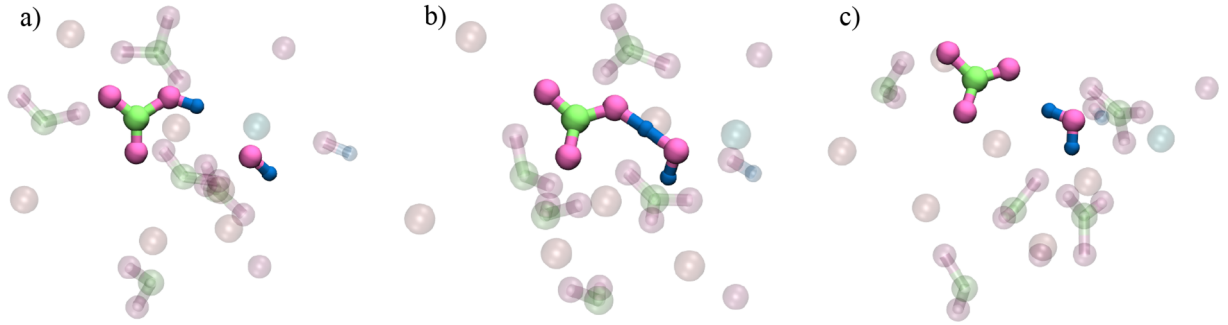

Figure 5. Snapshots representing the proton transfer between bicarbonate and hydroxide ions in AIMD simulation: (a) HCO_3^- and OH^- approach, (b) adduct formed, and (c) dissociation into CO_3^{2-} and H_2O. Color scheme: C = lime; O = mauve; H = blue. The rest of the atoms are shown as a transparent background for clarity.

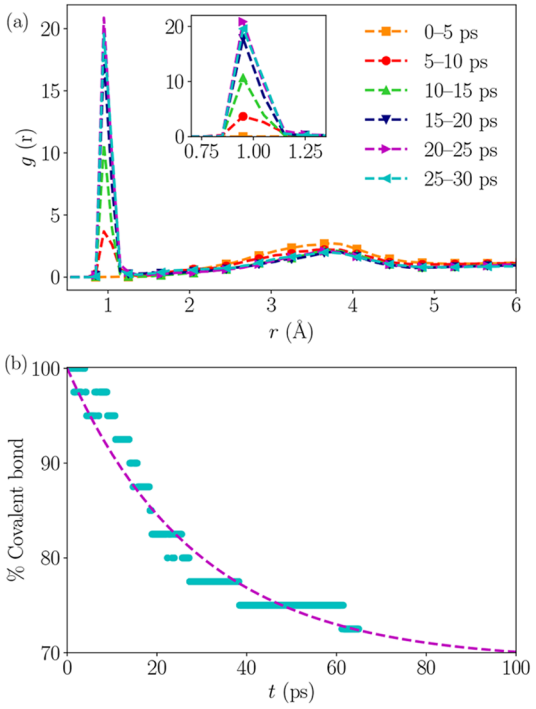

Figure 6. (a) Radial distribution functions between the hydrogen atom of OH^- and the oxygen atom of another OH^-. Intramolecular distances are ignored. (b) Percent covalent bond retained as a function of time: O−H bond in hydroxide ions present at $t = 0$.

This feature around 0.98 Å presents two possibilities: First, a proton is transferred from a bicarbonate ion to a hydroxide ion (Figure 5). Second, an H−O covalent bond forms where a proton (H^+) transfer between a water molecule and neighboring OH^-.

$$H_2O + OH^- \rightleftharpoons OH^- + H_2O \quad (8)$$

Thus, a water molecule undergoes a proton exchange reaction with a neighboring hydroxide moiety. This repeats itself, generating a sequence of proton transfer events as an exchange from one hydroxide to the next and can be compared to proton transfer via the Grotthuss mechanism observed in other systems.[34−41] To further substantiate the proposed mechanism, we computed the percent H−O covalent bond retained in the original OH^- as a function of time and shown in Figure 6b. As can be seen, the profile exhibits an exponential decay and therefore in association with Figure 6a certainly demonstrates that a proton leaves the oxygen in water and forms a new covalent bond with another oxygen in a neighboring hydroxide. Eventually, all H−O covalent bonds in the hydroxide ions present in the starting configuration would break provided that the simulated AIMD trajectory is sufficiently long.

The proton exchange mechanism is depicted sequentially in Figure 7a−c. As we can see, the proton transfer takes place via the formation of an intermediate ion, $H_3O_2^-$ (Figure 7b). These intermediate dimers are found to be stable for less than a picosecond on average before they break and re-form new dimers that results in proton transfer events. The formation of the $H_3O_2^-$ ion resembles the way OH^- moves through liquid

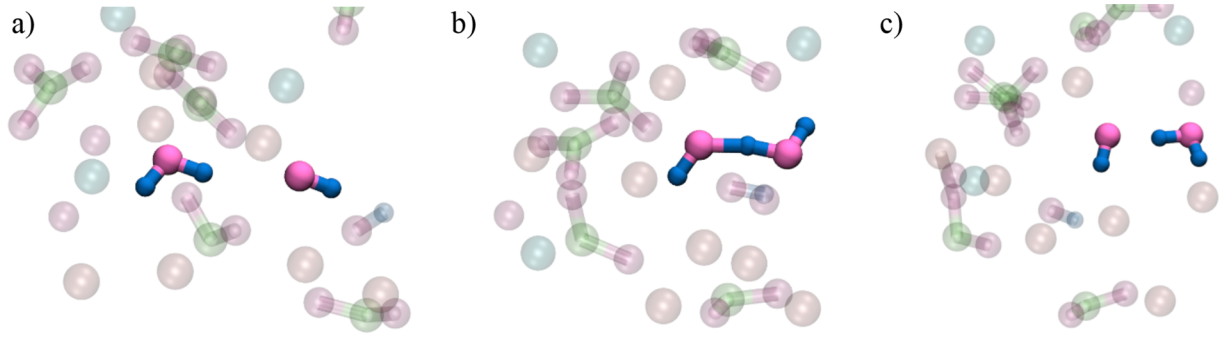

Figure 7. Snapshots representing water mediated proton transfer during AIMD simulation: (a) H_2O and OH^- approach, (b) formation of an $H_3O_2^-$ intermediate, and (c) transfer of H^+ to OH^-. Color scheme: O = mauve; H = blue. The rest of the atoms are shown as a transparent background for clarity.

https://dx.doi.org/10.1021/acs.jpcc.0c10879
J. Phys. Chem. C 2021, 125, 4412−4422

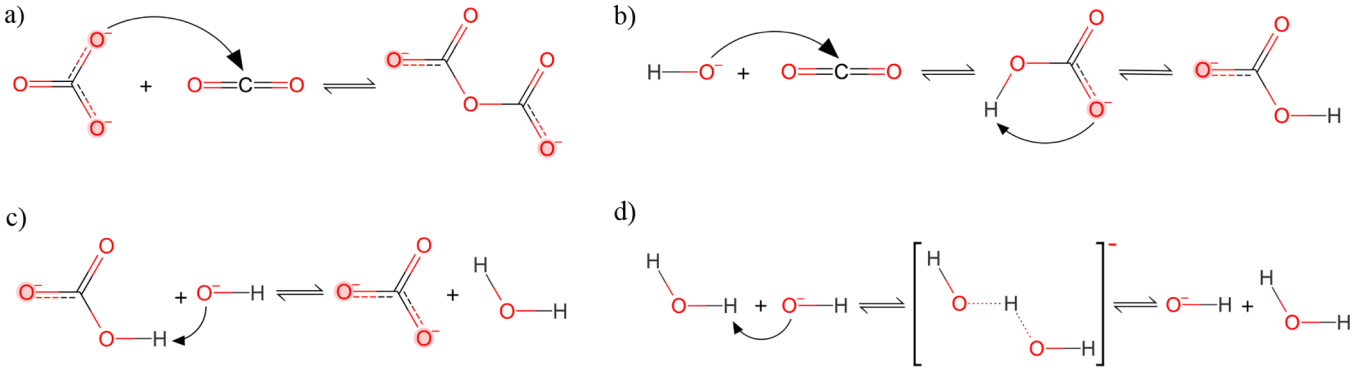

Figure 8. Summary of the different routes of chemical reactions undergoing in the system: (a) pyrocarbonate formation, (b) bicarbonate formation and isomerization, (c) proton transfer reaction between bicarbonate and hydroxide ions, and (d) proton transfer reaction between water and hydroxide anion via the formation of $H_3O_2^-$ intermediate.

water where the proton transfer process has been described as a stepwise hopping of a proton from a water molecule to an OH^- within a time frame of 1−2 ps.[35,39] Here, the proton transfers are aided by the fluctuations in the local electronic environment of molecular water in the molten electrolyte medium. Another intriguing fact of this mechanism is that the proton transfer does not take place in the pure electrolyte, as confirmed from the AIMD trajectory of a pure $[Li_{0.6}K_{0.4}]_3CO_3OH$ melt. Therefore, CO_2 molecules present in the electrolyte act as a catalyst. First they trigger the formation of bicarbonate (reaction with OH^-) that in turn donates a proton to a neighboring OH^- and generates a subsequent chain of proton exchange events. An interesting quantity to evaluate would be the contribution of the protons to the total conductivity of system. The presence of such spontaneous exchange events should lead to a significant level of proton conductivity (function of water concentration), which is of course higher than the conductivity arising from the normal diffusion of other ions. Therefore, at this elevated temperature (923.15 K) and in the presence of CO_2 (or H_2O), we should expect a higher conductivity of the system than without proton transfer events. A quantitative estimation is provided in a following section.

Evolution of Composition. The formation of molecular/ionic species via different chemical routes is summarized in Figure 8. To define a molecular species from the AIMD trajectory, it is necessary to use a distance criterion usually determined by looking at the minimum of the RDFs. We used two criteria for C−O and H−O covalent bonds based on their respective RDFs. A carbon atom was considered to be chemically attached to an oxygen atom if their separation was less than or equal to 1.8 Å, while the distance cutoff used for an H−O bond was 1.3 Å. The bonds between atoms were tracked between frames to determine when a new bond was formed or an existing bond broken. We used this breadth-first search algorithm to define similarly the other chemical species based on a particular distance criterion.

With the aforementioned criteria we observed the presence of pyrocarbonate, bicarbonate, and water, along with CO_3^{2-}, OH^-, and CO_2 in the simulation box, as shown in Figure 9. The points in the figure are the observed numbers in the simulation box at picosecond intervals, while the lines are drawn to guide the eye and highlight the overall trends. Initially, we began with 80 CO_3^{2-}, 40 OH^-, and 10 CO_2 molecules along with the alkali-metal cations. As it is evident from Figure 9, within the first picosecond of the simulation, the

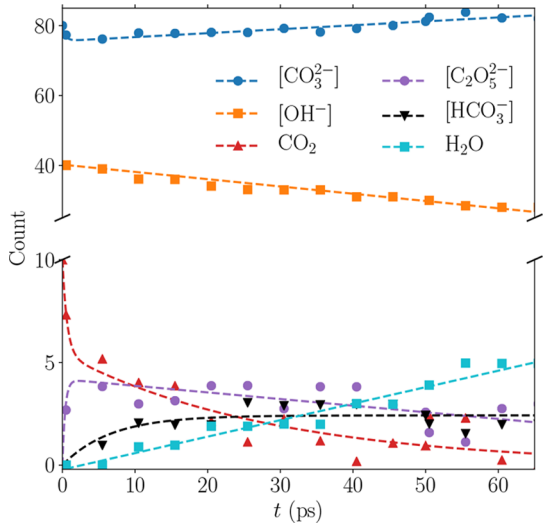

Figure 9. Number of different chemical species present as a function of time during the AIMD trajectory. Points are the actual observed numbers in the simulation box, while the lines are drawn to guide the eye.

carbonate and CO_2 counts were quickly reduced with the concomitant formation of pyrocarbonate ions. This suggests that pyrocarbonate formation from the reaction between CO_2 and CO_3^{2-} is the fastest chemical reaction in the system. The first appearance of a HCO_3^- ion was around 4 ps and H_2O around 10 ps. This transformation is part of the equilibrium reaction between bicarbonate and hydroxide ions (Figure 5). We also saw the presence of a constantly increasing amount of water accompanied by a steady level of bicarbonate and a depletion in pyrocarbonate ions as a function of time. The initial instant pyrocarbonate formation causes its concentration to dominate over that of bicarbonate and water for the first 40 ps of the trajectory, followed by a fall in the pyrocarbonate concentration.

Recall the decline in the growth of RDF peaks corresponding to pyrocarbonate formation beyond 25 ps (Figure 1a). In addition, the C−O covalent bonds in carbonate ions (Figure 1b) exhibit a much slower decay than that of H−O bonds in hydroxide ions (Figure 6b). Put together, these observations imply a decline in the growth of the pyrocarbonate fraction after an initial period of time and certainly reveal that pyrocarbonate formation as being kinetically favored whereas bicarbonate (and/or water) is the more thermodynamically

https://dx.doi.org/10.1021/acs.jpcc.0c10879
J. Phys. Chem. C 2021, 125, 4412−4422

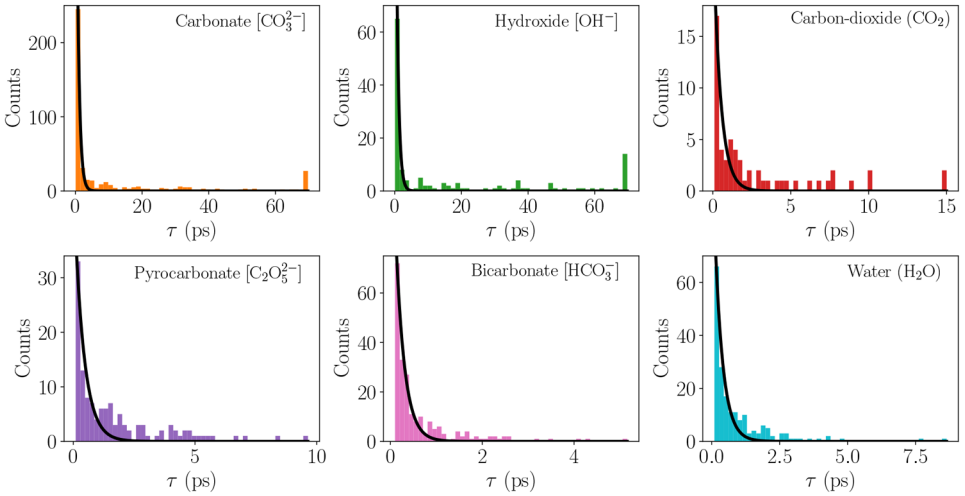

Figure 10. Lifetimes of different chemical species found during the AIMD trajectory. The black lines represent an exponential fit, $f(\tau) = ae^{-b\tau}$, to the lifetime distributions.

stable product. Also, the higher propensity of CO_2 undergoing a chemical reaction with OH^- (stronger base) than that of CO_3^{2-} (weaker base) is demonstrated by the difference in peak heights observed in Figure 1a vs Figure 3a. This difference can be explained in terms of the shift in the equilibrium of the CO_2−OH^- reaction more toward the right (eq 6). Once a bicarbonate ion forms, it undergoes a proton transfer reaction with a neighboring hydroxide, as indicated in eq 7. As a consequence, the equilibrium of the CO_2−OH^- reaction shifts toward the right and more bicarbonate is formed. On the other hand, a chemical reaction between a CO_2 and CO_3^{2-} leading to a pyrocarbonate ion (eq 5) does not undergo another subsequent transformation. Instead, there exists a dynamic equilibrium between the pyrocarbonate formation and dissociation.

Another important comparison is made in terms of the difference in the water and CO_2 concentrations in the melt. In our earlier work on chemical reaction equilibrium simulations using classical force fields, we showed that the concentration of dissolved water is over 2 orders of magnitude higher than that of CO_2 in a $[Li_{0.6}K_{0.4}]_3CO_3OH$ electrolyte over a wide range of CO_2 gas phase partial pressures.[9] The contrast in the dissolved concentrations was primarily justified as water being a polar molecule and having the ability to form hydrogen bonds, thus being more stable in the melt of oxidic ions. The present study also reveals a similar distinction in the concentration of water and CO_2 in the $[Li_{0.6}K_{0.4}]_3CO_3OH$ melt based on an *ab initio* molecular dynamics approach. Even though we started with a composition of 10 CO_2 and no water molecules in the system, the water fraction became higher than that of CO_2 within ∼35 ps of simulation time (Figure 9). Moreover, the water concentration remained almost twice as high (or sometimes higher) than that of the CO_2 for most of the rest of the simulation trajectory. The present quantitative investigation of water and CO_2 fractions reinforces the observation made previously from empirical force field calculations and certainly manifests the fact that water is more soluble than CO_2 in this or similar electrolytes with different alkali-metal cation compositions.

Overall, we observe a slow reduction in the hydroxide fraction whereas the number of CO_3^{2-} ions shows an initial depletion followed by a net gain over the simulation trajectory. This phenomenon can be explained as the dissociation of HCO_3^- producing a CO_3^{2-} and water and also the dynamic interplay between the pyrocarbonate formation and dissociation (Figure 2). The presence of more than one molecular water implies the possibility of multiple proton transfer chains between the hydroxide ions. Note that although Figure 9 provides important insights into the quantitative aspects of the different chemical species present during the AIMD trajectory, these numbers cannot be treated as the equilibrium values. This is primarily because all the different chemical reactions observed are coupled to each other, and as a consequence the system requires more time to attain an equilibrium than our simulations could cover. In addition, the composition of the gas phase that would be in equilibrium with this electrolyte is unknown and may be unrealistic for a real MCFC or other applications.

Species Lifetime. We used the same distance criteria and the breadth-first search algorithm as discussed in the previous section to evaluate the lifetimes of all the species quantified in Figure 9. The distributions of their lifetimes are shown in Figure 10. The histograms plotted in Figure 10 consider only those species that have lived at least 100 fs before dissociating into their constituent ions or atoms. This particular condition has been incorporated to avoid all those numerous short-lived intermediates that exist as a result of continuous formation/dissociation of chemical bonds before a complete transfer/event could take place.

Let us first look at the distributions of those species that are present at the beginning of the simulation, namely, CO_3^{2-}, OH^-, and CO_2. As it is evident from Figure 10, there are a number of CO_3^{2-} and OH^- ions that have not undergone any chemical transformation during the simulation period and have lived throughout the ∼70 ps trajectory. One would expect this phenomenon based on the analysis of percent covalent bond retained as a function of time (Figures 1b and 6b). On the contrary and more interestingly, the maximum lifetime of a molecular CO_2 is found to be around 15 ps. Therefore, within 15 ps all the CO_2 molecules present in the system have participated in chemical reactions with either a carbonate or hydroxide ion.

We investigated the distributions of lifetimes of species that appeared as a product of different chemical reactions, such as

https://dx.doi.org/10.1021/acs.jpcc.0c10879
J. Phys. Chem. C 2021, 125, 4412−4422

$C_2O_5^{2-}$, HCO_3^-, and H_2O. We found that both pyrocarbonate and water live up to maximum ~10 ps while bicarbonate exhibits a maximum lifetime of ~5 ps. We have also computed the weighted average lifetime of these species, and the numbers are as follows: hydroxide, 17.7 ps; carbonate, 12.9 ps; CO_2, 2.9 ps; pyrocarbonate, 1.8 ps; water, 1.0 ps; and bicarbonate, 0.7 ps. A low average lifetime of water implies that H_2O molecules diffuse not too far before finding another OH^- to react with, which subsequently leads to successive proton transfer from one OH^- site to the next. Also, we observe a contrasting behavior in the lifetime and concentration of CO_2 and water along the course of the AIMD trajectory. CO_2 exhibits a longer average lifetime (2.9 ps) than that of water (1.0 ps), whereas the concentration of water is found to be almost twice as high (or sometimes higher) than that of CO_2 beyond a threshold period (Figure 9). This distinction could be justified as the difference in the polarizability between water and CO_2. Being a polar molecule, water is expected to be more polarizable under this ionic environment than the nonpolar CO_2 molecule and thus would undergo chemical reactions spontaneously as compared to CO_2. A more detailed analysis of structural parameters such as bond lengths and angles in these two molecules and their deviation from ideal values can shed light onto the polarizability differences and is given in the following section. Also, one should remember that in our simulation the starting configuration is composed of a high concentration of CO_2 which may contribute to its higher average lifetime than the molecular water, which emerged as a product only after 10 ps simulation. Another important aspect of lifetime distributions is that beside CO_3^{2-} and OH^-, the remaining species possess a very short average lifetime with the maximum value of 2.9 ps for CO_2. Because those two ions are present in large concentrations and their counts do not change drastically over the period of simulation, one could imagine that the system would not take too long before reaching equilibrium provided that the other species have significantly shorter lifetimes.

As we discussed in previous sections, several chemical reactions occur spontaneously in the system as summarized in Figure 8. It is hard to treat these reactions independently since they are taking place simultaneously in the electrolyte and are coupled to each other. Therefore, to estimate the rate of individual events (the rate of formation/dissociation of a particular species), one should solve this coupled set of equations. Another option could be to fit an exponential function to the lifetime distribution of each chemical species, shown in Figure 10. The lifetimes incorporate all the different possibilities of formation/dissociation of an individual species. Thus, the exponential fit parameters to those distributions would provide an estimate of coupled rate of events. We have chosen a simple exponential function, $f(\tau) = ae^{-b\tau}$, to fit the lifetime distributions in Figure 10. The resultant parameters are tabulated in Table S1.

We found that bicarbonate exhibits the highest magnitude of b followed by water, pyrocarbonate, CO_2, OH^-, and CO_3^{2-}. Therefore, the frequency of events involving HCO_3^- formation and dissociation is the highest among all the species present in the electrolyte followed by same order in the b values. This order further substantiates the higher propensity of CO_2 reacting with OH^- as compared to CO_3^{2-}, also discussed in the previous sections.

Impact on the Dynamics. One of the important and compelling observations from the AIMD simulation of a $[Li_{0.6}K_{0.4}]_3CO_3OH$ electrolyte in the presence of CO_2 is the proton exchange from a water to a hydroxide ion. The presence of frequent proton transfer events would point toward a change in the mechanism of ion transport when CO_2 or H_2O is dissolved in the melt. To demonstrate this, we performed classical MD simulations of a $[Li_{0.6}K_{0.4}]_3CO_3OH$ eutectic mixture at the same hydroxide concentration and similar simulation conditions. The details of the simulations and models used are reported in another work.[21] From these simulations, we computed the diffusion coefficients of hydroxide (D_{OH^-}) and carbonate ($D_{CO_3^{2-}}$) ions, and their values are 0.129 and 0.054 Å^2/ps, respectively. Although estimating these diffusion coefficients from the AIMD trajectory should be possible in principle, the simulation time of <100 ps is not long enough to obtain reliable values. Now, if we consider the typical proton transfer distance (d_{PT}) between a water molecule and a hydroxide anion to be around 1 Å, then the time scale associated with a hydroxide ion diffusing this distance would be of the order of 7.75 ps [$\tau = 1/(D_{OH^-}/d_{PT}^2)$]. On the other hand, from the total number of proton transfer count over the whole trajectory, we found the proton transfer time scale to be around 0.6−0.7 ps. Therefore, the difference between these two time scales implies that the hydroxide diffusion is much slower (an order of magnitude at least) than a proton transfer event. As a consequence, the ion dynamics obtained from a classical force field (without explicit representation of electronic degrees of freedom) would be slower when compared to the actual value.

To provide a quantitative estimate of how much the proton exchange mechanism contributes to the proton conductivity, we employed a three-dimensional random walk model. The proton diffusion coefficient is then $D_{PT} = l^2/6\tau$, where l is the characteristic proton transfer distance and τ being the time scale associated with successive exchange events. We consider for l the nearest-neighbor distance between hydroxides in the melt, giving a value of ~3.75 Å. For the time between successive exchange events we use the value of $\tau = 0.6$ ps. The computed value of proton diffusion coefficient from this random walk model is thus $D_{PT} = 3.91$ Å^2/ps. Therefore, when compared to the diffusion coefficient of hydroxide, $D_{OH^-} = 0.129$ Å^2/ps (obtained from classical MD simulations at the same temperature and pressure), we conclude that the proton transport through the exchange mechanism is about 30 times faster. It is important to note here that the 30 times increase can be an overestimation, since it may take time for the water molecules to diffuse to a new hydroxide before the next proton transfer to occur; the exchange could also be back to the originating water molecule, resulting in little net motion. Nevertheless, we expect the proton transport in this MCFC electrolyte to play a significant role that could be the topic of future studies.

In a similar way, we estimated the contribution of the oxo-Grotthuss mechanism to the CO_2 transport. For this purpose, we take for l the nearest-neighbor distance between carbonates in the electrolyte, giving a value of ~4 Å. On the other hand, the typical time scale associated with the pyrocarbonate formation/dissociation is $\tau \sim 2.2$ ps (obtained from a count of the total number of pyrocarbonate formations over the whole trajectory). Using these values of jump distance and time scale, the computed value of the Grotthuss diffusion coefficient for CO_2 from the random walk model is $D_{Grotthuss}^{CO_2} = 1.21$ Å^2/ps, which is 20 times faster than the CO_3^{2-} diffusion obtained from a classical MD trajectory at the same temperature and

https://dx.doi.org/10.1021/acs.jpcc.0c10879
J. Phys. Chem. C 2021, 125, 4412−4422

pressure. The estimated value of Grotthuss diffusion coefficient, $D^{CO_2}_{Grotthuss}$, also agrees well with the similar quantity measured by Corradini et al. (0.83 Å^2/ps) in a $CaCO_3$−CO_3 system at 1773 K.[14]

Structural Analysis. The distributions of bond lengths and angles in instantaneous CO_2 and H_2O during the course of AIMD trajectory are computed and shown in Figure 11. As

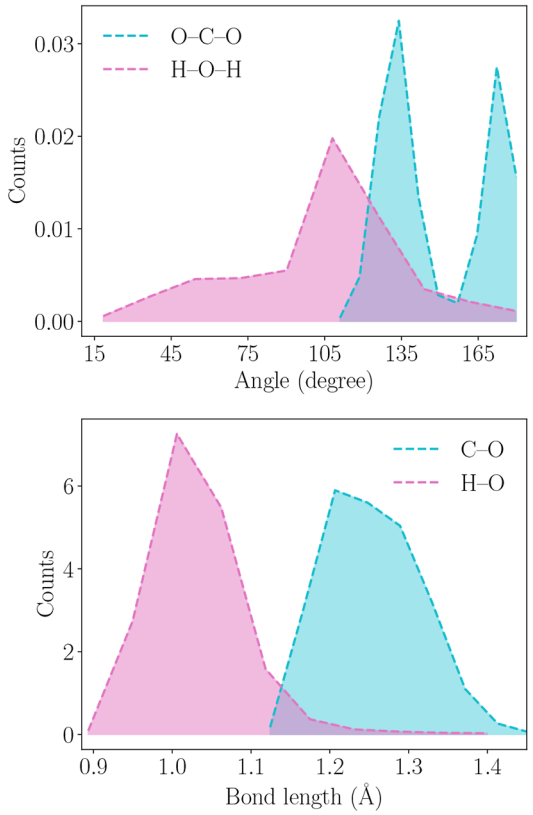

Figure 11. Top panel: distributions of O−C−O and H−O−H angles in CO_2 and H_2O. Bottom panel: distributions of C−O and H−O distances in CO_2 and H_2O.

evident, the fluctuations in the bond lengths, H−O in H_2O and C−O in CO_2, are comparable. The mean values of H−O and C−O distances in the condensed phase are 1.0 and 1.23 Å versus the gas phase values of 0.96 and 1.16 Å. The fluctuations of the O−C−O angle in CO_2 are significant and exhibit a bimodal distribution with sharp peaks. Despite the low polarizability of CO_2, we see here that the interactions with the surrounding medium, in this case composed of charged cations and anions, can influence deeply the geometry of CO_2. The peak around 135° can be related to those CO_2 molecules that are in the process of forming either pyrocarbonate or bicarbonate, whereas the other peak close to 180° corresponds to molecular CO_2. Similar distortion of the CO_2 geometry was also reported in the molten $CaCO_3$−CO_2 system by Corradini et al.[14] On the other hand, the fluctuations in the H−O−H angle in H_2O are even larger compared to those of the O−C−O angle in CO_2 in the melt. The magnitude of the H−O−H angle can be as low as ∼15° with a maximum value of ∼179°. A couple of representative snapshots with extreme water geometries are displayed in Figure S4. In particular, the bending of the H−O−H angle in H_2O can be attributed to its interaction with the neighboring hydroxide ion and participation in the proton transfer process. Therefore, in the melt, the geometry of H_2O is more affected by the surrounding ionic environment than that of CO_2. This phenomenon can be explained since H_2O is more polar and more polarizable than CO_2. The higher polarizability and consequently larger geometry distortion in H_2O explain its lower average lifetime than that of CO_2 in the melt, even though the concentration of H_2O is found to be approximately double that of CO_2.

CONCLUSIONS

The present AIMD simulations of CO_2 dissolved in a molten $[Li_{0.6}K_{0.4}]_3CO_3OH$ found that the molten phase contains pyrocarbonate, bicarbonate, and water along with the constituent ions and CO_2. We have observed a dynamic equilibrium between the pyrocarbonate formation and dissociation (eq 5) that facilitates the Grotthuss transport of CO_2 in the electrolyte medium.[14] Furthermore, we have discerned the interaction between CO_2 and hydroxide leading to the formation of bicarbonate (eq 6). Our results show that the bicarbonate proton undergoes an exchange process (exchange of covalent bonds with adjacent oxygen sites) before a complete transfer could take place to a hydroxide oxygen, resulting in a molecular water and another carbonate as the product (eq 7). Subsequently, the water molecule participates in a spontaneous proton transfer reaction with another hydroxide (eq 8) and generates a sequence of proton transfer events as an exchange from one hydroxide to the next. We found that the proton transfer process in the system follows a similar mechanism as the one observed for OH^- moving through liquid water via the formation of an $H_3O_2^-$ intermediate.[35,39] Recently, Drexler et al.[42] reported that Li^+ enhances proton delocalization as compared to Na^+ in aqueous alkali hydroxide solutions. Therefore, it would be interesting to investigate whether the proton transfer process is similarly affected by the alkali-metal countercations in molten salt mixtures.

Using distance-based criteria and a breadth-first search algorithm, we estimated the relative proportions of individual species found during the AIMD trajectory. Our results suggest a near-instantaneous formation and initial domination of pyrocarbonate over other species formed during the later course of the simulation. The pyrocarbonate fraction exhibits a slow decay at the later stage. Concomitantly, a constant increment is observed in the bicarbonate and water fraction. The presence of water in higher concentration than pyrocarbonate beyond an initial period manifests the kinetically fast $C_2O_5^{2-}$ formation, whereas water (and HCO_3^-) is the thermodynamically more favored product. The higher propensity of CO_2 to react with a OH^- rather than CO_3^{2-} is explained based on their relative basicity order, where the higher basicity of the former ion leads to its stronger binding affinity with CO_2, a Lewis acid. We also observed that the water concentration remains almost twice as high (or more) than that of the CO_2 beyond 35 ps, revealing a higher solubility of the former in the melt. These results reaffirm the observation made in our previous work based on chemical reaction equilibrium simulations.[9]

Overall, we found the following order in the average lifetime of the species present in the melt: OH^- > CO_3^{2-} > CO_2 > $C_2O_5^{2-}$ > H_2O > HCO_3^-. Surprisingly, CO_2 exhibits a higher magnitude of average lifetime (2.9 ps) than that of water (1.0 ps), although the concentration of the later dominated over the former for most of the simulation. We rationalize this by

https://dx.doi.org/10.1021/acs.jpcc.0c10879
J. Phys. Chem. C 2021, 125, 4412−4422

showing a larger geometry distortion of water (polar molecule) due to its higher polarizability than the distortion of the nonpolar CO_2. Consequently, water undergoes chemical reactions more spontaneously than CO_2.

The simulated results provide us important insights into the impact of proton transfer in the overall ion dynamics this electrolyte medium. We observe that the proton transport through exchange mechanism is about 30 times faster than the hydroxide diffusion calculated from classical MD simulations. Therefore, we should expect a higher magnitude of total conductivity than the one computed by using classical force fields.[21] We believe these simulation results will facilitate the fundamental understanding and development of electrolytes for various applications such as capacitors, batteries, and fuel cells.

■ ASSOCIATED CONTENT

Supporting Information

The Supporting Information is available free of charge at https://pubs.acs.org/doi/10.1021/acs.jpcc.0c10879.

Gas phase optimized geometry of ions, radial distribution function, and exponential fit parameters to the lifetime distributions (PDF)

■ AUTHOR INFORMATION

Corresponding Author

Athanassios Z. Panagiotopoulos − *Department of Chemical and Biological Engineering, Princeton University, Princeton, New Jersey 08544, United States;* orcid.org/0000-0002-8152-6615; Email: azp@princeton.edu

Authors

Anirban Mondal − *Department of Chemical and Biological Engineering, Princeton University, Princeton, New Jersey 08544, United States;* orcid.org/0000-0003-3029-8840

Jeffrey M. Young − *Department of Chemical and Biological Engineering, Princeton University, Princeton, New Jersey 08544, United States;* orcid.org/0000-0001-8879-5132

Gabor Kiss − *ExxonMobil Research and Engineering Co., Annandale, New Jersey 08801, United States*

Complete contact information is available at: https://pubs.acs.org/10.1021/acs.jpcc.0c10879

Notes

The authors declare the following competing financial interest(s): The Princeton authors declare no potential conflict of interest. Gabor Kiss, an employee of ExxonMobil Research and Engineering Co., is currently working on the applications of MCFCs in the industrial and power sectors.

■ ACKNOWLEDGMENTS

We thank Lucas Koziol for insightful discussions and a critical reading of manuscript. Financial support for this work was provided by ExxonMobil Research and Engineering Co., under Agreement EM09125.A1, and by the Office of Basic Energy Sciences, U.S. Department of Energy, under Award DE-SC0002128. Computing resources were provided by Princeton Research Computing.

■ REFERENCES

(1) Serrano-López, R.; Fradera, J.; Cuesta-López, S. Molten Salts Database for Energy Applications. *Chem. Eng. Process.* **2013**, *73*, 87−102.

(2) Caprile, L.; Passalacqua, B.; Torazza, A. Carbon Capture: Energy Wasting Technologies or the MCFCs Challenge? *Int. J. Hydrogen Energy* **2011**, *36*, 10269−10277.

(3) Wee, J.-H. Carbon Dioxide Emission Reduction Using Molten Carbonate Fuel Cell Systems. *Renewable Sustainable Energy Rev.* **2014**, *32*, 178−191.

(4) Hemmes, K.; Peelen, W. H. A.; de Wit, J. H. W. Study of the (Electro)Chemical Equilibria in Molten Carbonate Under the MCFC Cathode Gas Atmosphere. Part I: Selection of Independent Sets of Equilibria to Describe the (Electro)Chemical Equilibrium in Molten Carbonate Under the MCFC Cathode Gas Atmosphere. *Electrochim. Acta* **1998**, *43*, 2025−2031.

(5) Peelen, W. H. A.; van Driel, M.; Hemmes, K.; de Wit, J. H. W. Study of the (Electro)Chemical Equilibria in Molten Carbonate Under MCFC Cathode Gas Conditions. Part II: Non-Equilibrium Study of (Electro)Chemical Reactions Involved in Oxygen Reduction in Molten Carbonate. *Electrochim. Acta* **1998**, *43*, 3313−3331.

(6) Nishina, T.; Ohuchi, S.; Yamada, K.; Uchida, I. Water Effect on Oxygen Reduction in Molten (Li + K)CO_3 Eutectic. *J. Electroanal. Chem.* **1996**, *408*, 181−187.

(7) Evans, A.; Xing, W.; Norby, T. Electromotive Force (EMF) Determination of Transport Numbers for Native and Foreign Ions in Molten Alkali Metal Carbonates. *J. Electrochem. Soc.* **2015**, *162*, 1135−1143.

(8) Rosen, J.; et al. Molten Carbonate Fuel Cell Performance for CO_2 Capture from Natural Gas Combined Cycle Flue Gas. *J. Electrochem. Soc.* **2020**, *167*, 064505.

(9) Young, J. M.; Mondal, A.; Barckholtz, T. A.; Kiss, G.; Koziol, L.; Panagiotopoulos, A. Z. Predicting Chemical Reaction Equilibria in Molten Carbonate Fuel Cells via Molecular Simulations. *AIChE J.* **2020**, e16988.

(10) Audasso, E.; et al. New, Dual-Anion Mechanism for Molten Carbonate Fuel Cells Working as Carbon Capture Devices. *J. Electrochem. Soc.* **2020**, *167*, 084504.

(11) Audasso, E.; et al. The Effects of Gas Diffusion in Molten Carbonate Fuel Cells Working as Carbon Capture Devices. *J. Electrochem. Soc.* **2020**, *167*, 114515.

(12) Appleby, A. J.; Nicholson, S. B. Reduction of Oxygen in Alkali Carbonate Melts. *J. Electroanal. Chem. Interfacial Electrochem.* **1977**, *83*, 309−328.

(13) Chen, L. J.; Lin, C. J.; Zuo, J.; Song, L. C.; Huang, C. M. First Spectroscopic Observation of Peroxocarbonate/Peroxodicarbonate in Molten Carbonate. *J. Phys. Chem. B* **2004**, *108*, 7553−7556.

(14) Corradini, D.; Coudert, F. X.; Vuilleumier, R. Carbon Dioxide Transport in Molten Calcium Carbonate Occurs Through an Oxo-Grotthuss Mechanism via a Pyrocarbonate Anion. *Nat. Chem.* **2016**, *8*, 454−460.

(15) Hei, Y.; Huang, J.; Wang, C.; Mao, Z. Novel Doped Barium Cerate-Carbonate Composite Electrolyte Material for Low Temperature Solid Oxide Fuel Cells. *Int. J. Hydrogen Energy* **2014**, *39*, 14328−14333.

(16) Xiong, X.; Lei, X.; Zhang, C.; Wang, J.; Huang, K. Synergetic Proton Conduction in $BaZr_{0.8}Y_{0.2}O_{3-\delta}$-Carbonate Composite Electrolyte for Intermediate-Temperature Solid Oxide Fuel Cells. *Solid State Ionics* **2015**, *279*, 66−71.

(17) Lei, X.; Huang, K.; Qin, C. Proton Transfer in Molten Lithium Carbonate: Mechanism and Kinetics by Density Functional Theory Calculations. *Sci. Rep.* **2017**, *7*, 1−9.

(18) Spedding, P. L. Electrical Conductance of Molten Alkali Carbonate Binary Mixtures. *J. Electrochem. Soc.* **1973**, *120*, 1049.

(19) Hess, B.; Kutzner, C.; Van Der Spoel, D.; Lindahl, E. GROMACS 4: Algorithms for Highly Efficient, Load-Balanced, and Scalable Molecular Simulation. *J. Chem. Theory Comput.* **2008**, *4*, 435−447.

(20) Pronk, S.; et al. GROMACS 4.5: A High-Throughput and Highly Parallel Open Source Molecular Simulation Toolkit. *Bioinformatics* **2013**, *29*, 845−854.
(21) Mondal, A.; Young, J. M.; Barckholtz, T. A.; Kiss, G.; Koziol, L.; Panagiotopoulos, A. Z. Genetic Algorithm Driven Force Field Parameterization for Molten Alkali-Metal Carbonate and Hydroxide Salts. *J. Chem. Theory Comput.* **2020**, *16*, 5736−5746.
(22) Mondal, A.; Young, J. M.; Barckholtz, T. A.; Kiss, G.; Koziol, L.; Panagiotopoulos, A. Z. Transport and Interfacial Properties of Mixed Molten Carbonate/Hydroxide Electrolytes by Molecular Dynamics Simulations. *J. Phys. Chem. C* **2020**, *124*, 23532−23540.
(23) Hutter, J.; Iannuzzi, M.; Schiffmann, F.; VandeVondele, J. CP2K: Atomistic Simulations of Condensed Matter Systems. *Wiley Interdiscip. Rev.: Comput. Mol. Sci.* **2014**, *4*, 15−25.
(24) VandeVondele, J.; Krack, M.; Mohamed, F.; Parrinello, M.; Chassaing, T.; Hutter, J. Quickstep: Fast and Accurate Density Functional Calculations Using a Mixed Gaussian and Plane Waves Approach. *Comput. Phys. Commun.* **2005**, *167*, 103−128.
(25) Perdew, J. P.; Burke, K.; Ernzerhof, M. Generalized Gradient Approximation Made Simple. *Phys. Rev. Lett.* **1996**, *77*, 3865−3868.
(26) Grimme, S.; Antony, J.; Ehrlich, S.; Krieg, H. A Consistent and Accurate *Ab Initio* Parametrization of Density Functional Dispersion Correction (DFT-D) for the 94 Elements H-Pu. *J. Chem. Phys.* **2010**, *132*, 154104.
(27) Goedecker, S.; Teter, M.; Hutter, J. Separable Dual-Space Gaussian Pseudopotentials. *Phys. Rev. B: Condens. Matter Mater. Phys.* **1996**, *54*, 1703−1710.
(28) Hartwigsen, C.; Goedecker, S.; Hutter, J. Relativistic Separable Dual-Space Gaussian Pseudopotentials from H to Rn. *Phys. Rev. B: Condens. Matter Mater. Phys.* **1998**, *58*, 3641−3662.
(29) Martyna, G. J.; Tobias, D. J.; Klein, M. L. Constant Pressure Molecular Dynamics Algorithms. *J. Chem. Phys.* **1994**, *101*, 4177−4189.
(30) Martyna, G. J.; Klein, M. L.; Tuckerman, M. Nosé-Hoover Chains: The Canonical Ensemble via Continuous Dynamics. *J. Chem. Phys.* **1992**, *97*, 2635−2643.
(31) Solomons, T. W. G.; Fryhle, C. B.; Snyder, S. A. *Organic Chemistry*, 12th ed.; John Wiley & Sons, Inc.: Washington, DC, 2016.
(32) Mills, G. A.; Urey, H. C. The Kinetics of Isotopic Exchange between Carbon Dioxide, Bicarbonate Ion, Carbonate Ion and Water. *J. Am. Chem. Soc.* **1940**, *62*, 1019−1026.
(33) Middelburg, J. J. *Marine Carbon Biogeochemistry: A Primer for Earth System Scientists*; Springer International Publishing: Cham, 2019; pp 77−105.
(34) Marx, D.; Tuckerman, M. E.; Hutter, J.; Parrinello, M. The Nature of the Hydrated Excess Proton in Water. *Nature* **1999**, *397*, 601−604.
(35) Marx, D. Proton Transfer 200 Years after von Grotthuss: Insights from Ab Initio Simulations. *ChemPhysChem* **2006**, *7*, 1848−1870.
(36) Marx, D.; Chandra, A.; Tuckerman, M. E. Aqueous Basic Solutions: Hydroxide Solvation, Structural Diffusion, and Comparison to the Hydrated Proton. *Chem. Rev.* **2010**, *110*, 2174−2216.
(37) Knight, C.; Voth, G. A. The Curious Case of the Hydrated Proton. *Acc. Chem. Res.* **2012**, *45*, 101−109.
(38) Hassanali, A.; Giberti, F.; Cuny, J.; Kühne, T. D.; Parrinello, M. Proton Transfer Through the Water Gossamer. *Proc. Natl. Acad. Sci. U. S. A.* **2013**, *110*, 13723−13728.
(39) Codorniu-Hernández, E.; Kusalik, P. G. Probing the Mechanisms of Proton Transfer in Liquid Water. *Proc. Natl. Acad. Sci. U. S. A.* **2013**, *110*, 13697−13698.
(40) Chen, C.; Tse, Y. L. S.; Lindberg, G. E.; Knight, C.; Voth, G. A. Hydroxide Solvation and Transport in Anion Exchange Membranes. *J. Am. Chem. Soc.* **2016**, *138*, 991−1000.
(41) Ekimova, M.; Hoffmann, F.; Bekçioglu-Neff, G.; Rafferty, A.; Kornilov, O.; Nibbering, E. T.; Sebastiani, D. Ultrafast Proton Transport between a Hydroxy Acid and a Nitrogen Base along Solvent Bridges Governed by the Hydroxide/Methoxide Transfer Mechanism. *J. Am. Chem. Soc.* **2019**, *141*, 14581−14592.
(42) Drexler, C. I.; Miller, T. C.; Rogers, B. A.; Li, Y. C.; Daly, C. A.; Yang, T.; Corcelli, S. A.; Cremer, P. S. Counter Cations Affect Transport in Aqueous Hydroxide Solutions with Ion Specificity. *J. Am. Chem. Soc.* **2019**, *141*, 6930−6936.

https://dx.doi.org/10.1021/acs.jpcc.0c10879
J. Phys. Chem. C 2021, 125, 4412−4422